FISEVIER

Contents lists available at ScienceDirect

Journal of Alloys and Compounds

journal homepage: www.elsevier.com/locate/jalcom



The effects of Cu-substitution and high-pressure synthesis on phase transitions in Ni₂MnGa Heusler alloys



Jing-Han Chen^{a,*}, Tej Poudel Chhetri^a, Anthony T. Grant^a, Chung-Kai Chang^{b,*}, David P. Young^a, Igor Dubenko^c, Naushad Ali^c, Shane Stadler^a

- ^a Department of Physics and Astronomy, Louisiana State University, Baton Rouge, LA 70803, USA
- ^b National Synchrotron Radiation Research Center, Hsinchu 30076, Taiwan
- ^c Department of Physics, Southern Illinois University, Carbondale, IL 62901, USA

ARTICLE INFO

Article history:
Received 3 October 2021
Received in revised form 8 December 2021
Accepted 26 December 2021
Available online 29 December 2021

Keywords:
Phase transition
Heusler alloys
Magnetism
High pressure synthesis

ABSTRACT

The magnetic, structural, and thermal behaviors of the Cu-doped Heusler alloy $Ni_2Mn_{1-x}Cu_xGa$ ($0 \le x \le 0.4$) were studied as a function of concentration x. As the Cu concentration increased, the structural transition temperatures increased, whereas the chemical order-disorder transitions and melting points decreased. The experimental results from temperature dependent X-ray diffraction reveal different crystal structures of the martensite phase at low temperatures for samples with different x, but all the samples ultimately crystallized in the $L2_1$ cubic crystal structure upon heating above their respective structural transitions. The experimental data were used to construct a comprehensive magnetic and structural phase diagram as a function of x from below their respective structural transition temperatures to their melting temperatures. The XRD analysis shows that the observed volume reduction is associated with the increasing structural transition temperature. Therefore, one of the samples was annealed under high pressure to permanently reduce its volume, and the correlation between the increasing structural transition temperatures and volumes was confirmed.

© 2021 Elsevier B.V. All rights reserved.

1. Introduction

Interest in magnetic cooling technology has grown significantly due to advances in magnetic cooling devices based on materials that exhibit large magnetocaloric effects (MCEs) near room temperature [1,2]. An intensive effort has been made on understanding the physical mechanisms of the MCE, as well as designing better magnetocaloric materials. Giant MCEs often result from first-order magneto-structural transitions in solids and have been discovered in several systems, such as $Gd_5Si_{2-x}Ge_x$ [3], intermetallic MnTX (T = Co, Ni and X = Ge, Si) systems [4–7–10–13], MnAs-based compounds [14–16], Fe₂P-based compounds [17–20], and Ni₂MnZ-based (Z = In, Sn, Sb, orGa) Heusler alloys [21–24–27–30,31].

Among the magnetocaloric material candidates, considerable interest has been drawn specifically to Ni₂MnGa Heusler alloys since their magnetic and structural transitions occur close to room temperature, which is a requirement for devices operating at room temperature. At room temperature, Ni₂MnGa Heusler alloys

crystallize in the L2 $_1$ cubic structure and then transform to a martensite phase with lower symmetry at 200 K upon cooling [32]. On the other hand, the ferromagnetic ordering in Ni $_2$ MnGa Heusler alloys is destroyed through heating above its Curie temperature, 365 K. Upon further heating, the atomic order of Mn/Ga in the L2 $_1$ cubic structure is completely destroyed at 800 °C, above which a B2 cubic disordered phase forms [33]. In the L2 $_1$ cubic ordered phase, Mn and Ga atoms occupy two distinct locations, while in the B2 cubic disordered phase, Mn and Ga atoms are randomly distributed. The relationship between the L2 $_1$ cubic ordered phase and the B2 cubic disordered phase is illustrated in Fig. 1.

Given that the Mn atoms are known to dominate the magnetic interaction in Ni₂MnGa Heusler alloys [32], it has been recently shown that the Curie temperatures and structural transition temperatures can be simultaneously manipulated by partially substituting Mn atoms with V [35], Cr [36–38], Fe [39–41], Co [42–46], and Cu [43,46-54]. In Particular, for the composition Ni₂Mn_{1-x}Cu_xGa with x = 0.25, a giant MCE resulting from a coupled magneto-structural transition has been found [43,46,50,51,54]. Therefore, in this paper, we focus on polycrystalline alloys with the compositions Ni₂Mn_{1-x}Cu_xGa (0 $\leq x \leq$ 0.4) and systematically study their properties through magnetic, calorimetric, and temperature-dependent X-ray diffraction (XRD) measurements.

^{*} Corresponding authors. E-mail addresses: jhchen10@lsu.edu (J.-H. Chen), chang.ck@nsrrc.org.tw (C.-K. Chang).

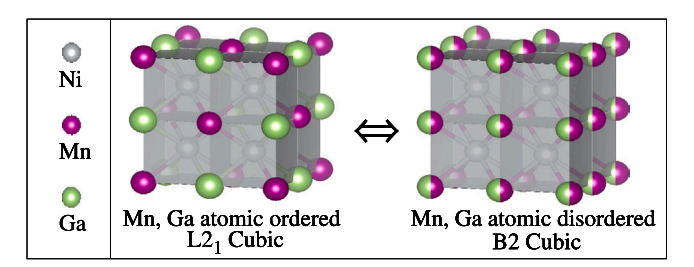


Fig. 1. The L2 $_1$ cubic ordered phase and the B2 cubic disordered phase are drawn in a polyhedral view by VESTA [34]. In the L2 $_1$ cubic ordered phase, Mn and Ga atoms occupy two distinct locations, while in the B2 cubic disordered phase, Mn and Ga atoms are randomly distributed.

It was observed that, as the Cu concentration in Ni₂Mn_{1-x}Cu_xGa increases, the structural transition temperatures increase, whereas the order-disorder transitions and melting temperatures decrease. Meanwhile, from temperature-dependent XRD measurements, it was found that the crystal structures of the martensite phase at low temperatures were different for different x, but all the samples ultimately crystallize in the L2₁ cubic structure upon heating above their respective structural transition temperatures. The experimental data were used to construct a comprehensive magnetic and structural phase diagram as a function of x from below their respective structural transition temperatures up to their melting temperatures. The XRD analysis shows that the observed volume reduction is associated with the increasing structural transition temperature. Therefore, one of the samples was annealed under high pressure (5.5 GPa) to permanently reduce its volume, and the correlation between the increasing structural transition temperatures and volumes was confirmed.

2. Sample preparation

Polycrystalline $\rm Ni_2Mn_{1-x}Cu_xGa$ alloy ingots (x=0,0.15,0.25,0.30,0.35, and 0.40) were fabricated from high purity (>99.95%) Ni, Mn, Cu, and Ga components by melting in a RF induction furnace in an Ar atmosphere. The samples in this paper are labeled as Cu-0 (x=0), Cu-15 (x=0.15), Cu-25 (x=0.25), Cu-30 (x=0.30), Cu-35 (x=0.35), and Cu-40 (x=0.40). The weight loss after melting was found to be less than 0.3% for each sample. The resulting as-cast ingots were first ground into powders. To ensure homogeneity and atomic order, as well as reduce the residual stress due to grinding, the samples were annealed at 700°C in $\rm Al_2O_3$ crucibles for 4 days in vacuum-sealed quartz tubes, and then slowly cooled to room temperature. Their respective magnetic, thermal, and structural properties are summarized in Table 1.

In addition, sample Cu-25 prepared as above was processed again under high pressure using a cubic multi-anvil high-pressure apparatus manufactured by Rockland Research Corporation[55]. The sample was ground and placed in a boron nitride crucible, surrounded with a graphite tube as the heater, and pyrophyllite was used as the pressure transmitting medium. This sample assembly was first compressed to a pressure of 5.5 GPa, and then heated to 1000 °C for 30 min. The temperature was then reduced to 700 °C, where it remained for 1 h. After these heating processes, the samples were slowly cooled to room temperature and then de-pressurized slowly. The experimental flow chart is illustrated in Fig. 2.

3. Thermal analysis

To reveal any possible phase transitions in our samples as a function of temperature, a simultaneous differential scanning calorimeter (DSC) and thermogravimetric analysis device (model: SDT Q600 manufactured by TA instruments, Inc.) was used. The experiments were performed by sweeping the temperature from room temperature through the melting points of all the samples. The results for sample Cu-25 are shown in Fig. 3 as a representative measurement. As the temperature increases from room temperature, the chemical order-disorder transition between L2₁ and B2 was detected at 738 °C, and the inset of Fig. 3 shows the result after background subtraction. Upon further heating, the first-order phase transition between the liquid phase and solid phase with thermal hysteresis was observed around 1150 °C.

The complete experimental results of the order-disorder transition temperature, and melting points, for all the samples are listed in Table 1 and are illustrated in Fig. 4. As the Cu concentration increases, the melting points (solid lines in Fig. 4) and order-disorder phase transitions (dashed lines in Fig. 4) decrease linearly. The lowest chemical order-disorder transition was observed for the sample with highest Cu concentration, i.e., Cu-40, which is 714.4 °C. Note that we chose 700 °C as the annealing temperature, which is below the chemical order-disorder transition for all the samples so that both chemical order and homogeneity can be promoted during the 4-day annealing process.

4. Magnetization measurements and analysis

The magnetization measurements were performed using a Magnetic Property Measurement System manufactured by Quantum Design within a temperature interval of 10–400 K, and in applied magnetic fields up to 7 T.

4.1. Temperature-dependent magnetization

The isofield temperature-dependent magnetization measurements were performed using field-cooled cooling and field-cooled warming protocols, the results of which are shown in Fig. 5 along with DSC data.

Table 1 Structural and magnetic parameters of $Ni_2Mn_{1-x}Cu_xGa$ as a function of concentration x.

label	composition Ni ₂ Mn _{1-x} Cu _x Ga	¹room temperature volume/f.u. (ų)	² structural transition	³ <i>T_{str.}</i> (K)	⁴ T _{L21} ↔ B2 (°C)	$^{5}M_{sat}/\text{f.u.} (\mu_{B})$	$\frac{6}{\partial T} \times 10^{-3} (\text{Å}^3/\text{K})$
Cu-0	x = 0.00	49.47	$10M \rightarrow L2_1$	210	797	4.25	2.10
Cu-15	x = 0.15	49.07	$10M \rightarrow L2_1$	256	760	3.51	2.02
Cu-25	x = 0.25	48.77	$14M \rightarrow L2_1$	311	738	3.06	2.03
Cu-30	x = 0.30	48.58	$D0_{22} \rightarrow L2_1$	365	726	2.92	2.67
Cu-35	x = 0.35	48.49	$D0_{22} \rightarrow L2_1$	438	720	2.68	2.74
Cu-40	x = 0.40	48.30	$D0_{22} \rightarrow L2_1$	503	714	2.41	2.83

- ¹ Estimated from X-ray diffraction experiments at room temperature as described in Sec. 5.1
- ² Obtained from the temperature-dependent X-ray diffraction experiments as described in Sec. 5.2
- 3 Structural transition temperature estimated from the magnetization or calorimetric experiments as described in Sec. 4.1
- ⁴ L21 ↔ B2 order-disorder transition temperature estimated from the calorimetric experiments as described in Sec. 3
- 5 Saturation magnetization estimated from the isothermal magnetization at 2 K as described in Sec. 4.2
- ⁶ Volume change rate estimated from temperature-dependent X-ray diffraction experiments as described in Sec. 5.2

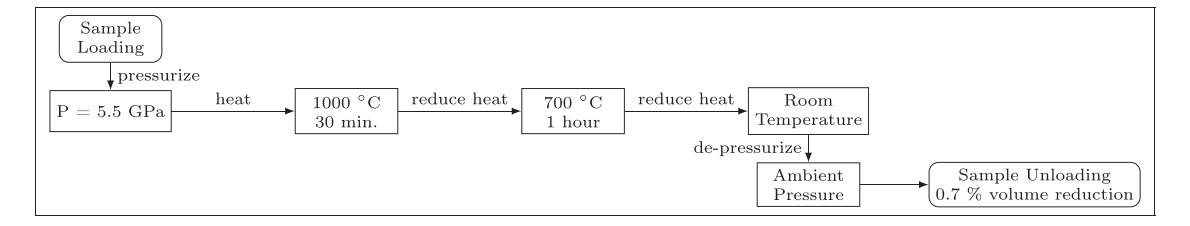


Fig. 2. Experimental high-pressure synthesis flow chart (sample Cu-25).

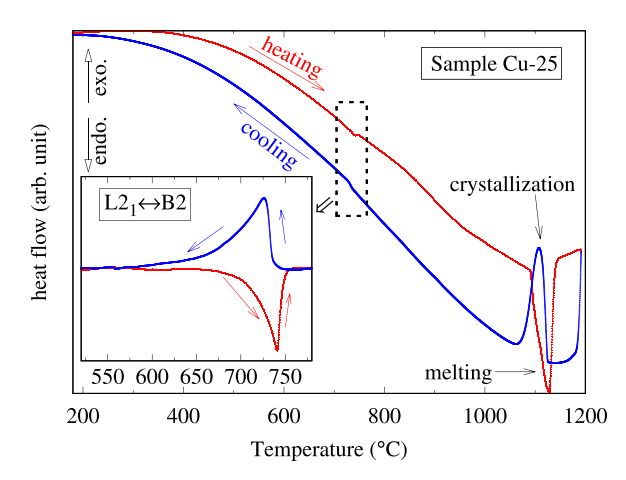


Fig. 3. The heat flow curves for sample Cu-25 are shown as a representative measurement. The temperature sweeping directions are indicated by arrows. The inset shows chemical order-disorder transitions between L2₁ and *B*2 phases at 738 °C after background subtraction. The first-order phase transition between the liquid phase and solid phases with thermal hysteresis was observed around 1150 °C.

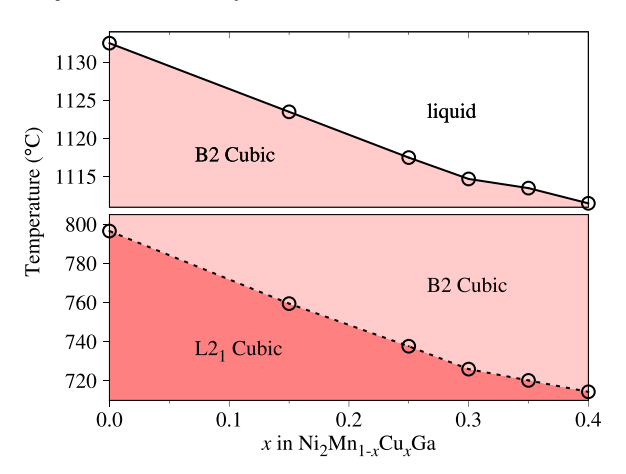


Fig. 4. A phase diagram mapping the chemical order-disorder transitions and melting points of $Ni_2Mn_{1-x}Cu_xGa$ ($x \le 0.4$) as a function of temperature and concentration x. As the Cu concentration increases, a linear decrease of the chemical order-disorder transition temperatures (dashed lines) and melting points (solid lines) was observed.

For samples Cu-0, Cu-15, Cu-25, and Cu-30, a clear thermal hysteresis due to first-order structural transitions was observed, and these structural transition temperatures becomes higher as the Cu concentration increases. For samples Cu-35 and Cu-40 (i.e. $x \ge 0.35$), their structural transition were in the paramagnetic region and were above 400 K so that calorimetric experiments were utilized for exploring their structural transitions, and the calorimetric results are shown in the upper right side of Fig. 5. In general, the structural transition temperatures increase as the Cu concentration increases, and a coupled magneto-structural transition was found for the sample Cu-25, which is consistent with previous reports [43,46,50,51,54]. The magnetic and structural transition information obtained from the above experiments are recorded in Table 1.

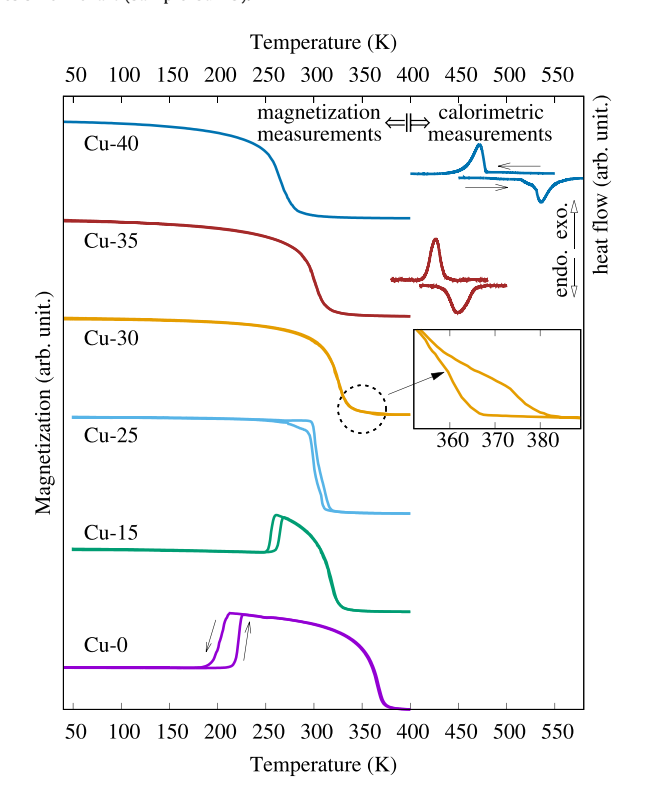


Fig. 5. The temperature-dependent magnetization of all the samples using field-cooled cooling and field-cooled warming protocols at $H = 1000\,\mathrm{Oe}$. For samples Cu-0, Cu-15, Cu-25, and Cu-30, a clear thermal hysteresis due to first-order structural transitions was observed in the magnetization results, and these structural transition temperatures shift to higher temperature as the Cu concentration increases. For samples Cu-35 and Cu-40 with structural transitions above 400 K, calorimetric experimental data are shown in the upper right side of this figure. The temperature sweeping directions indicated by arrows in the magnetization data of sample Cu-0 and calorimetric results of sample Cu-40 are representative of the corresponding sweeping procedure used on all the samples.

4.2. Field-dependent magnetization

To further investigate the magnetic properties of the samples at low temperature, saturation magnetization measurements at 2.0 K were performed in fields up to 7 T, as shown in the inset Fig. 6 (for samples Cu-0 and Cu-40).

The saturation magnetization (M_{sat}) values were estimated by fitting the experimental magnetization data using the law of approach-to-saturation

$$M(H) = M_{sat} \left(1 - \frac{a}{H^2} - \frac{b}{H^3} \right),$$

where a and b are fitting parameters [56,57]. The fitted M_{sat} values are listed in Table 1. Given that Mn atoms dominate the magnetic moments in the Ni₂Mn_{1-x}Cu_xGa alloy system, it is reasonable that the saturation moments decrease linearly as the Cu concentration increases and Mn concentration decreases, consistent with previous observations[32,53].

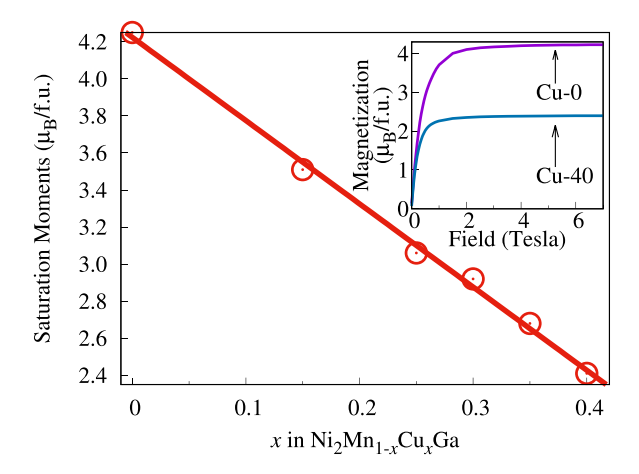


Fig. 6. Linear decrease of the saturation moments was observed as the Cu concentration increases. The inset shows the isothermal magnetization results for sample Cu-0 and Cu-40 at 2.0 K at ambient pressure which were performed in fields up to 7 Tesla.

5. Structural analysis by X-ray diffraction

X-ray diffraction (XRD) experiments were performed at beamline 11-BM, X-ray Science Division, the Advanced Photon Source, Argonne National Laboratory and at beamline TPS-19A, National Synchrotron Radiation Research Center, Taiwan. Room-temperature XRD was performed for the two Cu-0 samples, one of which was ground into powder before the heat treatment, whereas the other was ground after the heat treatment. A significant broadening of the peaks were found for the sample ground after the heat treatment as shown in Fig. 7. Since these materials are sensitive to grinding, the powder samples used in this paper were heat treated after grinding as described in Sec. 2.

5.1. Room temperature measurement

The powder XRD results at room temperature for all the samples are shown in Fig. 8 collected using an X-ray wavelength of 0.77489 Å.

For samples Cu-0, Cu-15, and Cu-25, L2₁ cubic crystal structures were observed. Samples with concentrations equal to or greater than 0.30 (i.e., Cu-30, Cu-35, and Cu-40) crystallized in a $D0_{22}$ tetragonal crystal structure, which is consistent with previous reports [58]. In addition, we observed that, as the Cu concentration x increased from 0.0 to 0.4, the volumes per formula unit decreased linearly, and the structural transition temperature increased as shown in Fig. 9.

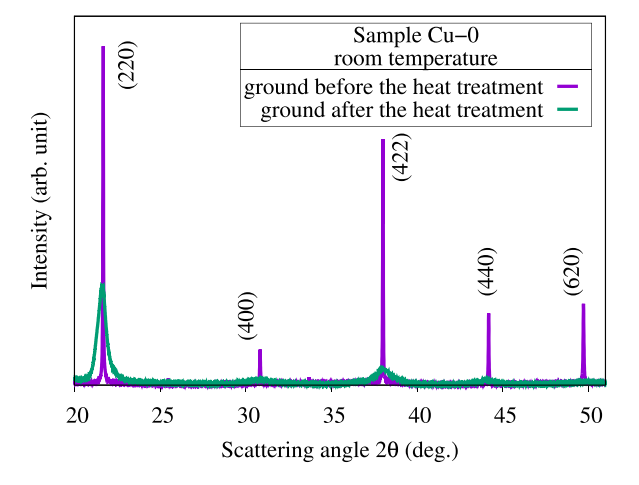


Fig. 7. Room-temperature XRD for the two Cu-0 powder samples, one of which was ground before the heat treatment, whereas the other was ground after the heat treatment. A significant broadening of the peaks was observed for the samples ground after the heat treatment.

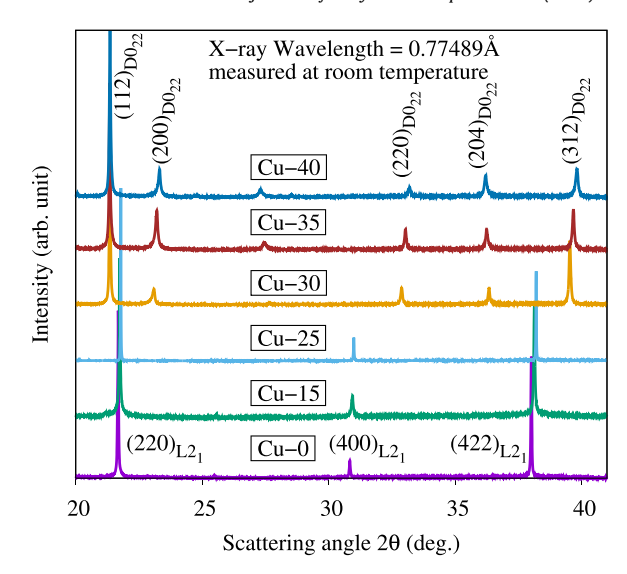


Fig. 8. Room-temperature powder X-ray diffraction patterns of all the samples using an X-ray wavelength of 0.77489 Å. For samples Cu-0, Cu-15, and Cu-25, L2₁ cubic crystal structures were observed. For the samples with $x \ge 0.3$ (i.e., Cu-30, Cu-35, and Cu-40), D0₂₂ tetragonal crystal structures were found. The corresponding Miller indices (in parentheses) of the L2₁ cubic and D0₂₂ tetragonal crystal structure are noted.

5.2. Temperature-dependent measurement

At room temperature, XRD measurements indicate that samples Cu-0, Cu-15, and Cu-25 all form in the L2₁ cubic crystal structure. As the temperature drops below their respective structural transitions, samples Cu-0 and Cu-15 assume the XRD pattern of a 10-layered (10 M) monoclinic crystal structure, which is similar to those previous observations [59–61], while sample Cu-25 shows the XRD pattern of a 14-layered (14 M) monoclinic structure, consistent with a previous published data [62]. The results for samples Cu-0, Cu-15, and Cu-25 at 100 K are shown in Fig. 10.

For the samples with $x \geqslant 0.3$ (i.e., Cu-30, Cu-35, and Cu-40), the D0₂₂ tetragonal structure was observed at room temperature. As the temperature increased above their respective structural transition temperatures, L2₁ cubic crystal structures were observed for these three samples. Generally speaking, all of the Ni₂Mn_{1-x}Cu_xGa (0 $\leqslant x \leqslant 0.4$) samples ultimately stabilized in L2₁ cubic crystal structures upon heating, although their martensite phases at low temperature each crystallized in different structures. The 10 M

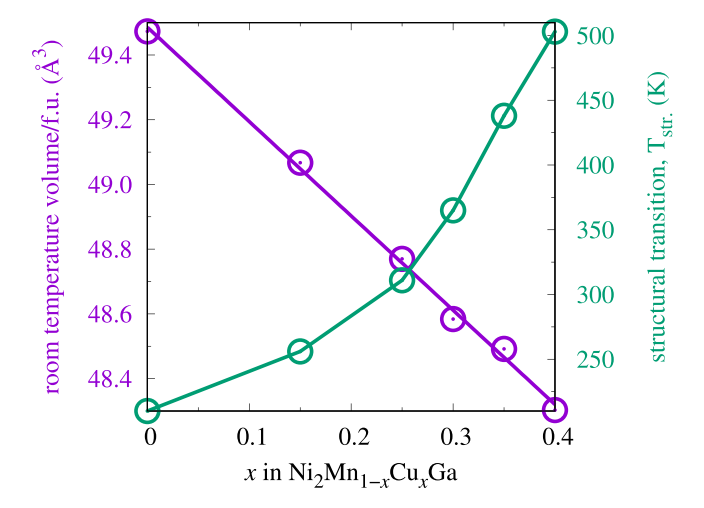


Fig. 9. The cell volume per formula unit at room temperature versus the Cu concentration *x*. As the Cu concentration increases, the volume reduces almost linearly and the structural transition temperature increases.

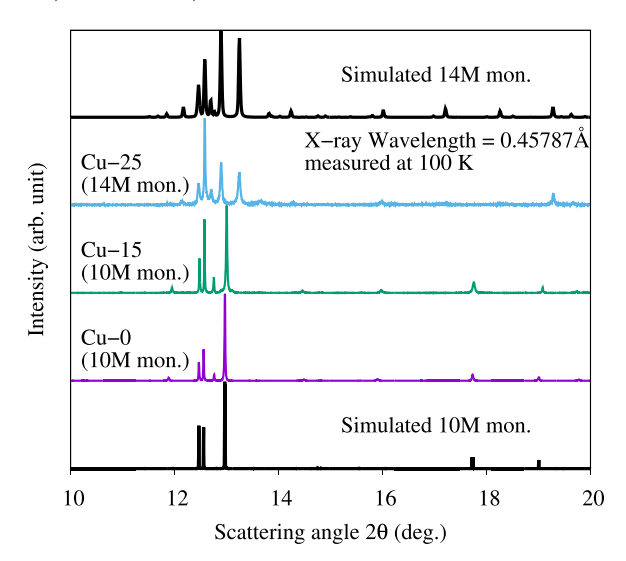


Fig. 10. X-ray diffraction patterns for samples Cu-0, Cu-15, and Cu-25 at 100 K. The X-ray wavelength was 0.45787 Åfor all measurements. The Cu-0 and Cu-15 samples assumed the XRD pattern of the 10-layered (10 M) monoclinic crystal structures, which is consistent with the previous findings [59–61], while sample Cu-25 shows the XRD pattern of the 14-layered (14 M) monoclinic structure, as reported in a previous work [62]. The simulated 10 M monoclinic and 14 M monoclinic XRD patterns are shown in the bottom and top panels, respectively.

monoclinic structure observed in Cu-0 and Cu-15, the 14 M monoclinic observed in Cu-25, and the $D0_{22}$ tetragonal structure observed in Cu-30, Cu-35, and Cu-40 can all be realized as a distortion of the $L2_1$ cubic structure along the (110) direction. The relationships between the 10 M monoclinic, 14 M monoclinic, $D0_{22}$ tetragonal, and $L2_1$ cubic structures are illustrated in Fig. 11.

The temperature-dependent volume changes across the structural transitions, calculated from XRD data, are shown in Fig. 12.

The usual linear dependence of the volume on the temperature was observed on both sides of the phase transition. The discontinuous volume changes as reported previously [50] is not apparent in this figure due to the scale and also that the XRD scans were measured by settling temperature instead of sweeping temperature across the transitions. The volume change rates for all the samples are listed in Table 1. By incorporating the temperature-dependent structural information, magnetization, and calorimetric

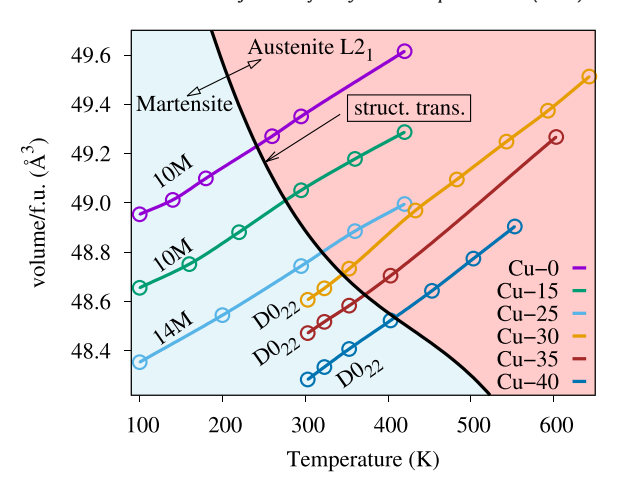


Fig. 12. Temperature-dependent cell volumes across the structural transitions calculated from XRD data. The volumes changed linearly with temperature on either of the transition.

measurements, a comprehensive structural and magnetic phase diagram was constructed and shown in Fig. 13. The magnetic and order-disorder transitions are second-order phase transitions and are shown as dashed lines, while the structural transitions and solid-liquid transitions (i.e., at the melting points) are first-order phase transitions and are shown as solid lines.

6. High pressure synthesis

Our XRD analysis indicates that the volume reduction with increasing Cu concentration is correlated with the increase of the structural transition temperature as shown in Fig. 9. Therefore, we chose sample Cu-25 as a case study to synthesize under high pressure in order to induce a volume reduction without changing its chemical composition. Sample Cu-25 was synthesized under high pressure by the method described in Sec. 2, and the cell volume of the resulting ingot calculated from XRD analysis was found to be reduced by 0.7%, which is consistent with our expectation since the samples were annealed under high pressure.

The temperature-dependent magnetization data collected using field-cooled cooling and field-cooled warming protocols at H = 10 Oe, and saturation magnetization measurements at 2.0 K were performed in fields up to 7 T are shown in Fig. 14. The experimental

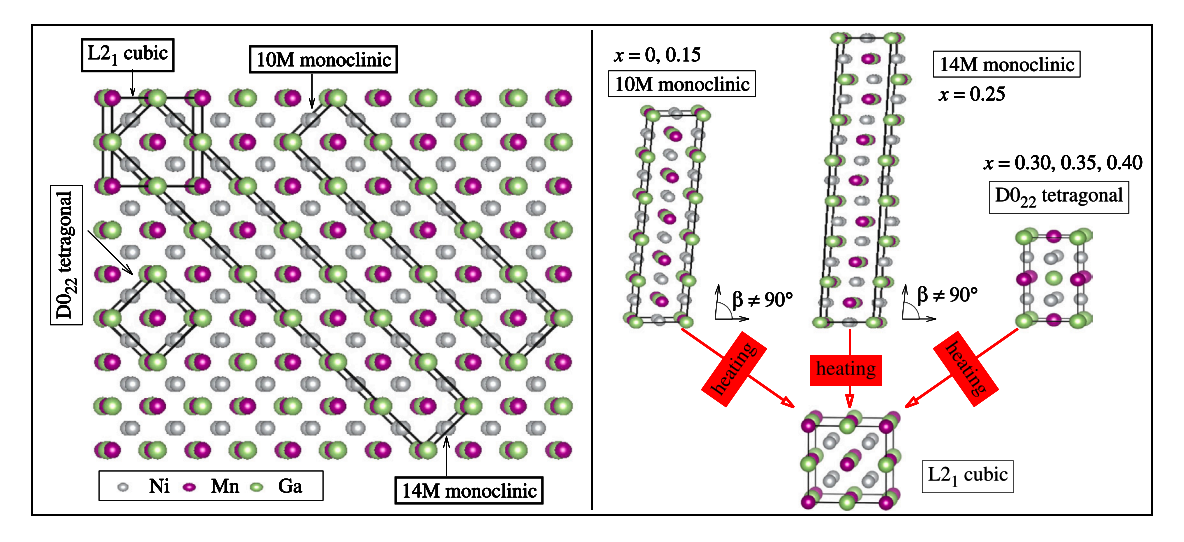


Fig. 11. (Left) A 4×5 set of L2₁ stoichiometric Ni₂MnGa cubic unit cells is shown to illustrate the relationship between 10 M monoclinic, 14 M monoclinic, D0₂₂ tetragonal, and L2₁ structures. (Right) The 10 M monoclinic, 14 M monoclinic, and D0₂₂ tetragonal structures can be interpreted as distortions of the L2₁ cubic structure along the (110) direction. Upon heating, the 10 M monoclinic, 14 M monoclinic, and D0₂₂ tetragonal structures transform to a L2₁ cubic structure.

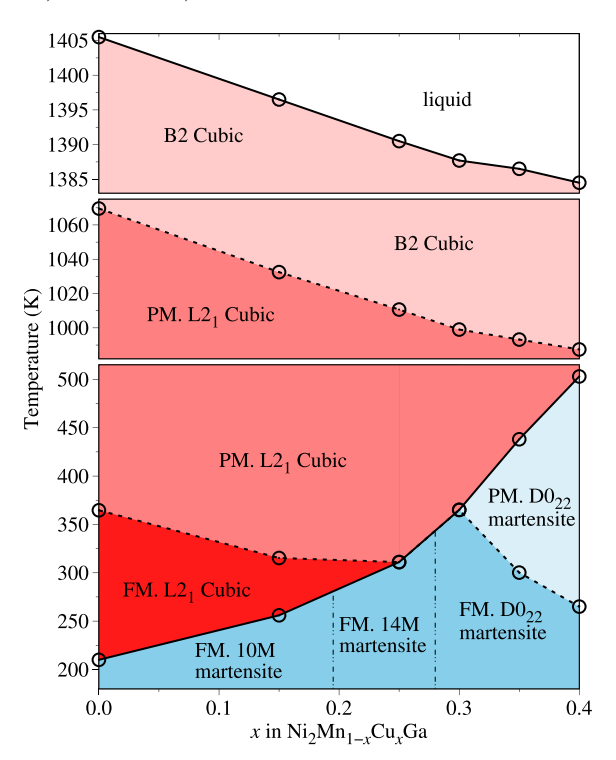


Fig. 13. A comprehensive phase diagram illustrating the magnetic, structural, order-disorder transitions, and melting points in Ni₂Mn_{1-x}Cu_xGa ($x \le 0.4$) Heusler alloys. The magnetic and order-disorder transitions are second-order phase transitions and are shown as dashed lines. The structural transitions and melting points (i.e., solid-liquid transitions) are first-order phase transitions and are shown as solid lines in the bottom and top panels, respectively.

results show that a higher structural transition temperatures were observed for the samples synthesized under high pressure while their saturation magnetizations were nearly unchanged.

The effect of the increasing structural transition temperature was induced by doping Cu for Mn in the Ni_2MnGa Heusler alloy, which causes the reduction of both volume and saturation magnetization. However, high-pressure synthesis offers the advantage of designing the materials without modifying their chemical compositions. In our specific case, the resulting increase in the structural transition temperature was induced only by reducing the cell volume, and hence chemical composition as well as the saturation magnetization were preserved.

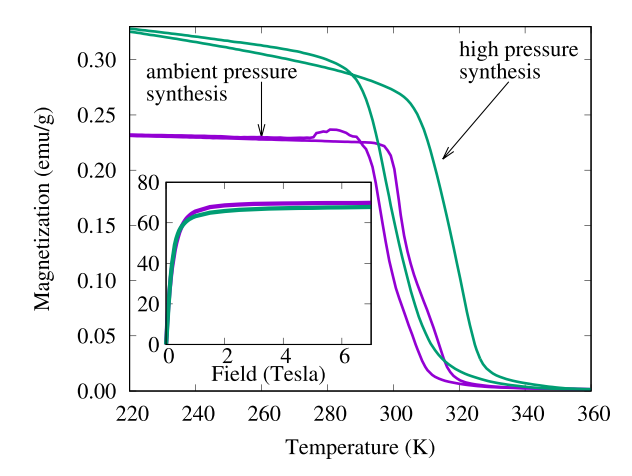


Fig. 14. Temperature-dependent magnetization of sample Cu-25 using field-cooled cooling and field-cooled warming protocols at $H = 10 \, \text{Oe}$. The experimental results show that the samples synthesized under high pressure had a higher transition temperature and larger thermal hysteresis, while their saturation magnetizations (inset) were nearly unchanged.

7. Conclusions

Systematic magnetization, temperature-dependent X-ray diffraction, and calorimetric measurements were performed on the Cudoped Heusler alloys Ni₂Mn_{1-x}Cu_xGa ($0 \le x \le 0.4$) in order to understand the functional properties of this alloy system. The main findings are summarized as follows: (i) the structural transition temperatures in Ni₂MnGa increased with increasing Cu concentration, and a positive correlation between the crystal volume and structural transition temperature was found. (ii) A comprehensive magnetic and structural phase diagram up to the melting points was constructed from direct experimental measurement, which not only elucidates the evoluation of the phase transitions for fundamental studies but also provides a practical guideline for material design purposes. (iii) High-pressure synthesis was employed to fabricate Ni₂Mn_{0.75}Cu_{0.25}Ga Heusler alloys, which preserves the chemical compositions of the samples, and hence solidified the connection between crystal volume and phase transition temperatures.

CRediT authorship contribution statement

Jing-Han Chen: Conceptualization, Methodology, Writing – original draft, Software, Validation, Formal analysis, Investigation, Visualization, Investigation. Tej Poudel Chhetri: Methodology, Writing – review & editing. Anthony T. Grant: Methodology, Writing – review & editing. Chung-Kai Chang: Methodology, Resources, Software, Data curation, Investigation. David P. Young: Methodology, Resources, Funding acquisition, Writing – review & editing. Naushad Ali: Resources, Funding acquisition, Writing – review & editing. Shane Stadler: Resources, Funding acquisition, Writing – review & editing, Investigation, Supervision, Project administration.

Declaration of Competing Interest

The authors declare that they have no known competing financial interests or personal relationships that could have appeared to influence the work reported in this paper.

Acknowledgments

S. Stadler acknowledges support from the U.S. Department of Energy, Office of Basic Energy Sciences under Award No. DE-FG02-13ER46946. N. Ali and I. Dubenko acknowledge support from the U.S. Department of Energy, Office of Basic Energy Sciences under Award No. DE-FG02-06ER46291. D. P. Young acknowledges support from the U.S. National Science Foundation, Division of Materials Research under Award No. NSF-DMR-1904636. This research used resources of the Advanced Photon Source, a U.S. Department of Energy (DOE) Office of Science User Facility operated for the DOE Office of Science by Argonne National Laboratory under Contract No. DE-AC02-06CH11357. The DSC data used in this work were collected at the Center for Advanced Microstructures and Devices under the supervision of A. Roy. Jing-Han Chen gratefully acknowledges Robert J. Cava and Kelly Powderly at Princeton University, and Valentin Taufour at the University of California, Davis for sharing their experience with the high pressure synthesis apparatus.

References

- C. Zimm, A. Jastrab, A. Sternberg, V.K. Pecharsky, K.A. Gschneidner Jr., M. Osborne, I. Anderson, Description and Performance of a Near-Room Temperature Magnetic Refrigerator 43 Springer, US, Boston, MA, 1998, pp. 1759–1766.
- [2] V. Provenzano, A.J. Shapiro, R.D. Shull, Reduction of hysteresis losses in the magnetic refrigerant Gd₅ Ge₂ Si₂ by the addition of iron, Nature 429 (6994) (2004) 853–857.
- [3] V.K. Pecharsky, K.A. Gschneidner Jr., Giant Magnetocaloric Effect in Gd₅ Si₂ Ge₂, Phys. Rev. Lett. 78 (1997) 4494–4497.

- [4] J.-H. Chen, T. PoudelChhetri, C.-K. Chang, Y.-C. Huang, D.P. Young, I. Dubenko, S. Talapatra, N. Ali, S. Stadler, The influence of hydrostatic pressure and annealing conditions on the magnetostructural transitions in MnCoGe, J. Appl. Phys. 129 (2021) 215108.
- [5] V. Johnson, C.G. Frederick, Magnetic and crystallographic properties of ternary manganese silicides with ordered Co₂ P structure, Phys. Status Solidi (a) 20 1973) 331-335
- (1975) V. Johnson, Diffusionless orthorhombic to hexagonal transitions in ternary silicides and germanides, Inorg. Chem. 14 (1975) 1117–1120.
- [7] I. Liu, Y. Si, Y. Gong, G. Xu, E. Liu, F. Xu, D. Wang, Enhanced magnetic refrigeration performance in metamagnetic MnCoSi alloy by high-pressure annealing, J. Alloy. compd. 701 (2017) 858-863.
- [8] K. Morrison, A. Barcza, J.D. Moore, K.G. Sandeman, M.K. Chattopadhyay, S.B. Roy, A.D. Caplin, L.F. Cohen, The magnetocaloric performance in pure and mixed
- magnetic phase CoMnSi, J. Phys. D: Appl. Phys. 43 (2010) 195001. S. Anzai, K. Ozawa, Coupled nature of magnetic and structural transition in MnNiGe under pressure, Phys. Rev. B 18 (1978) 2173–2178.
- [10] W. Bażela, A. Szytuła, J. Todorović, Z. Tomkowicz, A. Zięba, Crystal and magnetic structure of NiMnGe, Phys. Status Solidi (a) 38 (1976) 721–729.
- [11] H. Fjellvåg, A.F. Andresen, On the crystal structure and magnetic properties of MnNiGe, J. Magn. Magn. Mater. 50 (1985) 291–297.
- [12] C.F. Sánchez-Valdés, J.L. SánchezLlamazares, H. Flores-Zúñiga, D. Ríos-Jara, P. Alvarez-Alonso, Pedro Gorria, Magnetocaloric effect in melt-spun MnCoGe
- ribbons, Scr. Mater. 69 (2013) 211–214.

 [13] V.K. Sharma, M.A. Manekar, H. Srivastava, S.B. Roy, Giant magnetocaloric effect near room temperature in the off-stoichiometric Mn-Co-Ge alloy, J. Phys. D:
- Appl. Phys. 49 (2016) 50LT01.

 [14] H. Wada, Y. Tanabe, Giant magnetocaloric effect of MnAs_{1-x} Sb_x, Appl. Phys. Lett. 79 (2001) 3302–3304.
- [15] H. Wada, T. Morikawa, K. Taniguchi, T. Shibata, Y. Yamada, Y. Akishige, Giant magnetocaloric effect of MnA_{1-x} Sb_x in the vicinity of first-order magnetic transition, Phys. B 328 (2003) 114–116.
- L. Tocado, E. Palacios, R. Burriel, Adiabatic measurement of the giant magneto-caloric effect in MnAs, J. Therm. Anal. Calorim. 84 (2006) 213–217.
- [17] O. Tegus, E. Brück, K.H.J. Buschow, F.R.De Boer, Transition-metal-based magnetic refrigerants for room-temperature applications, Nature 415 (6868) (2002)
- [18] H. Fujii, T. Hōkabe, T. Kamigaichi, T. Okamoto, Magnetic properties of Fe₂ P single crystal, J. Phys. Soc. Jpn. 43 (1977) 41–46.
- [19] J.-H. Chen, K.H. Whitmire, A structural survey of the binary transition metal phosphides and arsenides of the d-block elements, Coord, Chem. Rev. 355 (2018)
- [20] P. Jernberg, A. Yousif, L. Häggström, Y. Andersson, A. Mössbauer, study of Fe₂ P_{1-x}
- SI_{x} ($x \le 0.35$), J. Solid State Chem. 53 (1984) 313–322. [21] J.-H. Chen, N.M. Bruno, I. Karaman, Y. Huang, J. Li, J.H. Ross Jr., Direct measure of giant magnetocaloric entropy contributions in Ni-Mn-In, Acta Mater. 105 (2016)
- [22] J.-H. Chen, N.M. Bruno, I. Karaman, Y. Huang, J. Li, J.H. Ross Jr., Calorimetric and magnetic study for Ni₅₀ Mn₃₆ In₁₄ and relative cooling power in paramagnetic inverse magnetocaloric systems, J. Appl. Phys. 116 (2014) 203901.
- [23] J.-H. Chen, N.M. Bruno, Z. Ning, W.A. Shelton, I. Karaman, Y. Huang, J. Li, J.H. Ross r., Relative cooling power enhancement by tuning magneto-structural stability in Ni-Mn-In Heusler alloys, J. Alloy. Compd. 744 (2018) 785-790.
- [24] A. Planes, L. Mañosa, M. Acet, Magnetocaloric effect and its relation to shapememory properties in ferromagnetic Heusler alloys, J. Phys.:Condens. Matter 21 2009) 233201
- [25] Y. Sutou, Y. Imano, N. Koeda, T. Omori, R. Kainuma, K. Ishida, K. Oikawa, Magnetic and martensitic transformations of NiMnX (X = In, Sn, Sb) ferromagnetic shape memory alloys, Appl. Phys. Lett. 85 (2004) 4358-4360.
- T. Krenke, E. Duman, M. Acet, E.F. Wassermann, X. Moya, L. Mañosa, A. Planes Inverse magnetocaloric effect in ferromagnetic Ni-Mn-Sn alloys, Nat. Mater. 4 (2005) 450-454.
- K. Oikawa, W. Ito, Y. Imano, Y. Sutou, R. Kainuma, K. Ishida, S. Okamoto, O. Kitakami, T. Kanomata, Effect of magnetic field on martensitic transition of Ni₄₆ Mn₄₁ In₁₃ Heusler alloy, Appl. Phys. Lett. 88 (2006) 122507.
- [28] M. Khan, N. Ali, S. Stadler, Inverse magnetocaloric effect in ferromagnetic Ni₅₀ Mn_{37+x} Sb_{13-x} Heusler alloys, J. Appl. Phys. 101 (2007) 053919.
 [29] F.S. Liu, Q.B. Wang, W.Q. Ao, Y.J. Yu, L.C. Pan, J.Q. Li, Magnetocaloric effect in high
- Ni content Ni_{52} Mn_{48-x} In_x alloys under low field change, J. Magn. Magn. Mater. 324 (2012) 514–518.
- [30] L.H. Bennett, V. Provenzano, R.D. Shull, I. Levin, E.D. Torre, Y. Jin, Ferri-to ferromagnetic transition in the martensitic phase of a Heusler alloy, J. Alloy. Compd. 525 (2012) 34–38.
- [31] T. Krenke, E. Duman, M. Acet, E.F. Wassermann, X. Moya, L. Mañosa, A. Planes, E. Suard, B. Ouladdiaf, Magnetic superelasticity and inverse magnetocaloric effect in Ni-Mn-In, Phys. Rev. B 75 (2007) 104414.
- [32] P.J. Webster, K.R.A. Ziebeck, S.L. Town, M.S. Peak, Magnetic order and phase transformation in Ni₂ MnGa, Philos. Mag. B 49 (1984) 295-310.
- [33] H. Ishikawa, R. Umetsu, K. Kobayashi, A. Fujita, R. Kainuma, K. Ishida, Atomic ordering and magnetic properties in Ni₂ Mn(Ga_x Al_{1-x}) Heusler alloys, Acta Mater. 56 (2008) 4789-4797.

- [34] K. Momma, F. Izumi, VESTA3 for three-dimensional visualization of crystal. volumetric and morphology data, J. Appl. Crytall. 44 (2011) 1272–1276.
- U. Devarajan, M. Kannan, R. Thiyagarajan, M.M. Raja, N.V.R. Rao, S. Singh, D. Venkateshwarlu, V. Ganesan, M. Ohashi, S. Arumugam, Coupled magnetostructural transition in Ni-Mn-V-Ga Heusler alloys and its effect on the magnetocaloric and transport properties, J. Phys. D: Appl. Phys. 49 (2015) 065001. [36] Y. Adachi, R. Kouta, M. Fujio, T. Kanomata, R.Y. Umetsu, X. Xu, R. Kainuma,
- Magnetic phase diagram of heusler alloy system $Ni_2 Mn_{1-x} Cr_x Ga$, Phys. Procedia 75 (2015) 1187–1191.
- [37] M. Khan, J. Brock, I. Sugerman, Anomalous transport properties of Ni₂Mn_{1-x}Cr_xGa heusler alloys at the martensite-austenite phase transition, Phys. Rev. B 93 2016) 054419.
- [38] T. Sakon, N. Fujimoto, T. Kanomata, Y. Adachi, Magnetostriction of Ni₂ Mn_{1-x} Cr_x Ga Heusler Alloys, Metals 7 (10) (2017).
- [39] Z.H. Liu, M. Zhang, W.Q. Wang, W.H. Wang, J.L. Chen, G.H. Wu, F.B. Meng, H.Y. Liu, B.D. Liu, J.P. Qu, Y.X. Li, Magnetic properties and martensitic transformation in quaternary Heusler alloy of NiMnFeGa, J. Appl. Phys. 92 (2002) 5006–5010.
- [40] J. Tróchez, J. Camargo, I. Piñeres, D. LandínezTellez, Effect of Fe on thermal and electrical properties in Ni₂ Mn_{1-x} Fe_x Ga Heusler alloys, Phys. B 558 (2019)
- [41] D. Kikuchi, T. Kanomata, Y. Yamaguchi, H. Nishihara, K. Koyama, K. Watanabe, Magnetic properties of ferromagnetic shape memory alloys $Ni_2 Mn_{1-x} Fe_x Ga$, J. Alloy. Compd. 383 (2004) 184–188.
- [42] A. Nespoli, C.A. Biffi, E. Villa, A. Tuissi, Effect of heating/cooling rate on martensitic transformation of NiMnGa-Co high temperature ferromagnetic shape memory alloys, J. Alloy. Compd. 690 (2017) 478–484.

 [43] M. Khan, I. Dubenko, S. Stadler, N. Ali, The structural and magnetic properties of
- Ni₂ Mn_{1-x} M_x Ga (M=Co, Cu), J. Appl. Phys. 97 (2005) 10M304.
- [44] M. Khan, S. Stadler, N. Ali, Intermartensitic transformations in Ni₂ Mn_{1-x} Co_x Ga
- Heusler alloys, J. Appl. Phys. 99 (2006) 08M705. [45] B. Bao, Y. Long, J.F. Duan, P.J. Shi, G.H. Wu, R.C. Ye, Y.Q. Chang, J. Zhang, C.B. Rong, Phase transition processes and magnetocaloric effect in Ni_{2.15} Mn_{0.85-x} Co_x Ga alloys, J. Appl. Phys. 103 (2008) 07B335.

 [46] A.M. Gomes, M. Khan, S. Stadler, N. Ali, I. Dubenko, A.Y. Takeuchi, A.P. Guimarães,
- Magnetocaloric properties of the Ni_2 Mn_{1-x} (Cu,Co)_x Ga Heusler alloys, J. Appl. Phys. 99 (2006) 08Q106.
- [47] C. Seguí, J. Torrens-Serra, E. Cesari, P. Lázpita, Optimizing the Caloric Properties of Cu-Doped Ni-Mn-Ga Alloys, Materials 13 (2) (2020). [48] A. Us Saleheen, J.-H. Chen, D.P. Young, I. Dubenko, N. Ali, S. Stadler, Critical be-
- havior in Ni₂ MnGa and Ni₂ Mn_{0.85} Cu_{0.15} Ga, J. Appl. Phys. 123 (2018) 203904. [49] Z. Li, N. Zou, C.F. Sánchez-Valdés, J.L.S. Llamazares, B. Yang, Y. Hu, Y. Zhang, C. Esling, X. Zhao, L. Zuo, Thermal and magnetic field-induced martensitic transformation in Ni₅₀ Mn_{25-x} Ga₂₅ Cu_x ($0 \le x \le 7$) melt-spun ribbons, J. Phys. D: Appl. Phys. 49 (2015) 025002.
- S. Stadler, M. Khan, J. Mitchell, N. Ali, A.M. Gomes, I. Dubenko, A.Y. Takeuchi, A.P.G. aes, Magnetocaloric properties of Ni₂ Mn_{1-x} Cu_x Ga, Appl. Phys. Lett. 88 (2006) 192511.
- [51] C. Jiang, J. Wang, P. Li, A. Jia, H. Xu, Search for transformation from paramagnetic martensite to ferromagnetic austenite: NiMnGaCu alloys, Appl. Phys. Lett. 95 (2009) 012501.
- [52] J.F. Duan, Y. Long, B. Bao, H. Zhang, R.C. Ye, Y.Q. Chang, F.R. Wan, G.H. Wu, Experimental and theoretical investigations of the magnetocaloric effect of Ni_{2.15}
- Mn_{0.85-x} Cu_x Ga (x = 0.05, 0.07) alloys, J. Appl. Phys. 103 (2008) 063911.
 [53] T. Kanomata, K. Endo, N. Kudo, R.Y. Umetsu, H. Nishihara, M. Kataoka, M. Nagasako, R. Kainuma, K.R. Ziebeck, Magnetic Moment of Cu-Modified Ni₂ MnGa Magnetic Shape Memory Alloys, Metals 3 (1) (2013) 114–122.
 [54] S. Roy, E. Blackburn, S.M. Valvidares, M.R. Fitzsimmons, S.C. Vogel, M. Khan,
- I. Dubenko, S. Stadler, N. Ali, S.K. Sinha, J.B. Kortright, Delocalization and hybridization enhance the magnetocaloric effect in Cu-doped Ni₂ MnGa, Phys. Rev.
- [55] P.D. McNutt, Cubic multi anvil device (U.S. Patent 6,022,206, Feb. 2, 2000).
- [56] A.H. Morrish, The Physical Principles of Magnetism, John Wiley & Sons, Inc., 2001
- B.D. Cullity, C.D. Graham, Introduction to Magnetic Materials, John Wiley & Sons, Inc., 2011.
- [58] M. Kataoka, K. Endo, N. Kudo, T. Kanomata, H. Nishihara, T. Shishido, R.Y. Umetsu, M. Nagasako, R. Kainuma, Martensitic transition, ferromagnetic transition, and their interplay in the shape memory alloys Ni₂ Mn_{1-x} Cu_x Ga, Phys. Rev. B 82 (2010) 214423.
- [59] L. Righi, F. Albertini, L. Pareti, A. Paoluzi, G. Calestani, Commensurate and in-commensurate "5M" modulated crystal structures in Ni-Mn-Ga martensitic phases, Acta Mater. 55 (2007) 5237-5245.
- [60] Z. Li, Y. Zhang, C. Esling, X. Zhao, L. Zuo, Twin relationships of 5M modulated martensite in Ni-Mn-Ga alloy, Acta Mater. 59 (2011) 3390–3397.
- L. Righi, F. Albertini, G. Calestani, L. Pareti, A. Paoluzi, C. Ritter, P.A. Algarabel, . Morellon, M. Ricardo Ibarra, Incommensurate modulated structure of the ferromagnetic shape-memory Ni₂ MnGa martensite, J. Solid State Chem. 179 (2006) 3525-3533
- [62] L. Righi, F. Albertini, E. Villa, A. Paoluzi, G. Calestani, V. Chernenko, S. Besseghini, C. Ritter, F. Passaretti, Crystal structure of 7M modulated Ni-Mn-Ga martensitic phase, Acta Mater. 56 (2008) 4529-4535.